

• Original Paper •

Assimilation of the FY-4A AGRI Clear-Sky Radiance Data in a Regional Numerical Model and Its Impact on the Forecast of the “21·7” Henan Extremely Persistent Heavy Rainfall[※]

Lan XU^{1,2}, Wei CHENG³, Zhongren DENG⁴, Juanjuan LIU^{1,2}, Bin WANG^{1,2},
Bin LU⁵, Shudong WANG⁶, and Li DONG^{1,2}

¹State Key Laboratory of Numerical Modeling for Atmospheric Sciences and Geophysical Fluid Dynamics,
Institute of Atmospheric Physics, Chinese Academy of Sciences, Beijing 100029, China

²College of Earth and Planetary Sciences, University of Chinese Academy of Sciences, Beijing 100049, China

³Beijing Institute of Applied Meteorology, Beijing 100029, China

⁴Key Laboratory of Meteorological Disaster of Ministry of Education (KLME)/Joint International
Research Laboratory of Climate and Environment Change (ILCEC), Nanjing University of
Information Science & Technology, Nanjing 210044, China

⁵Institute of Urban Meteorology, China Meteorological Administration, Beijing 100089, China

⁶Public Meteorological Service Center, China Meteorological Administration, Beijing 100081, China

(Received 27 September 2021; revised 23 December 2021; accepted 14 January 2022)

ABSTRACT

Assimilation of the Advanced Geostationary Radiance Imager (AGRI) clear-sky radiance in a regional model is performed. The forecasting effectiveness of the assimilation of two water vapor (WV) channels with conventional observations for the “21·7” Henan extremely heavy rainfall is analyzed and compared with a baseline test that assimilates only conventional observations in this study. The results show that the 24-h cumulative precipitation forecast by the assimilation experiment with the addition of the AGRI exceeds 500 mm, compared to a maximum value of 532.6 mm measured by the national meteorological stations, and that the location of the maximum precipitation is consistent with the observations. The results for the short periods of intense precipitation processes are that the simulation of the location and intensity of the 3-h cumulative precipitation is also relatively accurate. The analysis increment shows that the main difference between the two sets of assimilation experiments is over the ocean due to the additional ocean observations provided by FY-4A, which compensates for the lack of ocean observations. The assimilation of satellite data adjusts the vertical and horizontal wind fields over the ocean by adjusting the atmospheric temperature and humidity, which ultimately results in a narrower and stronger WV transport path to the center of heavy precipitation in Zhengzhou in the lower troposphere. Conversely, the WV convergence and upward motion in the control experiment are more dispersed; therefore, the precipitation centers are also correspondingly more dispersed.

Key words: FY-4A, AGRI, clear-sky radiance, satellite data assimilation, “21·7” Henan extremely persistent heavy rainfall

Citation: Xu, L., W. Cheng, Z. R. Deng, J. J. Liu, B. Wang, B. Lu, S. D. Wang, and L. Dong, 2023: Assimilation of the FY-4A AGRI clear-sky radiance data in a regional numerical model and its impact on the forecast of the “21·7” Henan extremely persistent heavy rainfall. *Adv. Atmos. Sci.*, **40**(5), 920–936, <https://doi.org/10.1007/s00376-022-1380-3>.

Article Highlights:

- AGRI clear-sky WV channels radiance is effectively assimilated in a regional high-resolution model.
- The location and intensity of both 24-h and 3-h cumulative precipitation with the assimilation of the AGRI are more accurate than without such assimilation.
- The FY-4A AGRI compensates for the lack of ocean observations and can improve the structure of atmospheric circulations.

※ This paper is a contribution to the special issue on the 14th International Conference on Mesoscale Convective Systems and High-Impact Weather.

* Corresponding author: Juanjuan LIU
Email: ljjxgg@mail.iap.ac.cn

1. Introduction

In recent years, disasters caused by extreme rainstorms have become more frequent. Several studies have shown that numerical weather prediction (NWP) has been greatly improved in recent decades and that regional numerical models with higher resolution are more effective in forecasting rainstorms triggered by small- and medium-scale weather (Mass et al., 2002; Charlton-Perez et al., 2015; Qi et al., 2020). In addition, with the improvement of satellite remote sensing capabilities and the development of fast radiative transfer models, most NWP centers have achieved direct assimilation of radiance data from various satellite instruments (Saunders et al., 1999; Thépaut, 2003; Matricardi et al., 2004; Collard, 2007; Weng, 2007; Zapotocny et al., 2007; Liu et al., 2009; Bauer et al., 2011; Xu et al., 2013; Eresmaa et al., 2017; Weng et al., 2020). In particular, geostationary satellite data, because of its high spatial and temporal resolution, can effectively complement observations over land and ocean and can improve the distribution of state variables such as model temperature and water vapor (WV) observations (Li et al., 2011; Lupu and McNally, 2011; Qin et al., 2013), which facilitates improved storm forecasting.

High temporal resolution data from geostationary satellites in regional numerical models provides more information than polar-orbiting satellites (also known as sun-synchronous orbiting satellites) in the same region. Compared with polar-orbiting meteorological satellites, which essentially observe the same region of the Earth twice a day, geostationary satellites have their own advantages, such as continuous observations of the same region at short intervals, which are invaluable for capturing rapidly evolving small- and meso-scale weather systems. Since 2014, the world officially entered the launch period of the second generation of geostationary meteorological satellites. The following geostationary satellites have been or will be launched: Japan's Himawari-8 and 9, the US GOES-16/17, Europe's Meteosat and China's Fengyun-4A (FY-4A) and 4B (Schmit et al., 2005; Bessho et al., 2016; Yang et al., 2017).

Research using the Advanced Baseline imager (ABI) on GOES-16/17, the Spinning Enhanced Visible and InfraRed Imager (SEVIRI) on Meteosat Second Generation (MSG), and the Advanced Himawari Imager (AHI) on Himawari-8 has found that assimilation of geostationary satellite imager data can improve numerical forecasts (Szyndel et al., 2005; Ma et al., 2017; Okamoto, 2017; Zou et al., 2017; Honda et al., 2018; Kazumori, 2018; Qin and Zou, 2018; Okamoto et al., 2019). Szyndel et al. (2005) used the four-dimensional variational data assimilation (4DVar) system of the European Centre for Medium-Range Weather Forecasts (ECMWF) to assimilate the clear-sky brightness temperature (BT) of SEVIRI WV channels and found that assimilation of WV radiance data was able to better adjust the simulated WV distribution. Cintineo et al. (2016) found that assimilating ABI WV brightness temperatures can improve the structure of the water vapor field in the clear-sky regions

and the analysis of cloud tops and produced better forecasts of the structure of severe convective storms. Wang et al. (2018) assimilated Himawari-8 AHI clear-sky WV radiance data to forecast the “7·19” severe storm of 2016 in North China and found that assimilating the AHI WV radiance data significantly improved the horizontal and vertical distribution characteristics in the moisture fields and was helpful for better forecasting the heavy rainstorm. Lu et al. (2019) found that impacts from assimilation of AHI WV information are dependent of cumulus parameterization (CP) and micro-physical scheme (MS), and can be optimized by combing appropriate CP and MS schemes. Xu et al. (2021) also assimilated Himawari-8 AHI WV radiance data but used all-sky data, and the assimilation also improved the location and intensity of rainfall forecasts.

The Advanced Geostationary Radiance Imager (AGRI) onboard China's new-generation geostationary satellite FY-4A has 14 channels and can scan every 5 minutes with a sub-satellite point resolution of 0.5–4 km (Yang et al., 2017). Compared with the Visible Infrared Spin-Scan Radiometer (VISSR) onboard geostationary satellite FY-2, the FY-4A AGRI has more spectral bands and higher temporal and spatial resolution to provide more accurate information on the state of the atmosphere. However, direct assimilation of the FY-4A AGRI datasets has not appeared yet in the literature. Some researchers have reported at academic conferences on the application of assimilation of FY4A AGRI WV channels radiance in the Global/Regional Assimilation and Prediction System (GRAPES) global model. Their results suggest that assimilation of the AGRI clear-sky WV channels made a weakly positive contribution to the moisture field in the middle troposphere of East Asia.

In this study, the assimilation of the AGRI clear-sky WV radiance in the Weather Research and Forecasting variational data assimilation (WRFDA) is implemented and the impact on storm forecasting is assessed for the case of the “21·7” Henan extremely heavy rainfall. Considering that there are very few space-time matched satellite data corresponding to heavy rainfall in high-resolution regional numerical models, this paper focuses on the impact of AGRI assimilation on the basis of conventional observations.

The subsequent sections are organized as follows. Section 2 describes the assimilation of the AGRI clear-sky radiance data in the regional numerical model. Section 3 presents the case of the “21·7” Henan extremely heavy rainfall, the data used and the experimental design. In section 4, the results based on the case study are analyzed. The discussion and conclusions are given in section 5.

2. The assimilation of the AGRI Clear-Sky Radiance data in WRFDA

2.1. Data assimilation system

The assimilation experiments in this paper are based on three-Dimensional Variational (3DVar) and the assimilation system is WRFDA v3.9. The Advanced Research WRF

v3.9.1 model (ARW-WRF) is used as the regional numerical forecast model. The assimilated conventional observational data and the physical parameter configuration of ARW-WRF are consistent with the Beijing Meteorological Bureau operational model (Zhong et al., 2020). The Radiative Transfer for the TIROS Operational Vertical Sounder (RTTOV; Eyre, 1991; Saunders et al., 1999) is used as the satellite radiance observation operator. The AGRI coefficient file is provided by NWP-SAF (<https://nwp-saf.eumetsat.int>). Based on these coefficients, RTTOV can simulate AGRI clear-sky radiances given vertical profiles of atmospheric temperature, water vapor, surface temperature and wind speed, solar and sensor geometry parameters and some other parameters.

Variational data assimilation (DA) requires that both the observation error and the background error can be characterized as unbiased Gaussian distributions (Dee, 2005). When performing direct DA of satellite data, the bias between the simulated BT and observed BT affects the accuracy of numerical prediction (Eyre, 1992; Harris and Kelly, 2001; McNally et al., 2006; Collard and McNally, 2009; Li et al., 2019). Therefore, this study uses the variational bias correction (VarBC) method to reduce bias in the direct assimilation process of the AGRI (Dee, 2004; Auligné et al., 2007). VarBC changes the observation operator by adding a correction term:

$$\tilde{H}(\mathbf{x}, \boldsymbol{\beta}) = \mathbf{H}(\mathbf{x}) + \sum_{i=0}^N \beta_i p_i(\mathbf{x}),$$

where $\mathbf{H}(\mathbf{x})$ and $\tilde{H}(\mathbf{x}, \boldsymbol{\beta})$ are the observation operators before and after the bias correction, respectively. \mathbf{x} represents the atmospheric state vectors. The p_i and β_i are the i -th predictor and the corresponding bias correction coefficients, respectively. In this study, p_i includes a constant component regarding 1000–300 hPa and 200–50 hPa layer thicknesses, surface skin temperature, and total column water.

2.2. FY-4A AGRI radiance data

The AGRI includes 14 channels in the visible, near-

infrared and infrared (IR) spectral bands. The spectral coverage, spectral bands, spatial resolution, and main applications for each channel are given in Table 1 (Yang et al., 2017). The AGRI has a high temporal resolution, completing a full-disk observation in approximately 15 minutes, providing one full-disk image every 1 hour, three consecutive full-disk images every 3 hours (a total of 40 full-disk images per day), and one image of the Chinese region every 5 minutes when full-disk observations are not being made.

Figure 1 shows the Jacobian functions of temperature and WV for the AGRI IR channels using standard atmosphere by RTTOV (Channels 1–7 are not shown due to the poor simulation capability of the radiative transfer model for visible and near-infrared bands). The Jacobian functions denote the change of top-of-atmosphere (TOA) radiance in response to perturbations in either the atmosphere or surface state (Di et al., 2016). In Fig. 1, it is illustrated that the ch9 and ch10 of AGRI are sensitive to both the WV in the 100–200 hPa layer and the temperature in the 400–600 hPa layer. These two channels are WV absorption channels, and the bias between the observed BT and the BT simulated by the model is also relatively small (Geng et al., 2020). In addition, it has been shown that WV channels can provide more accurate information on moisture, which is very important for the simulation of severe rainstorm events. Therefore, only the two WV channels, ch9 and ch10, are assimilated in the subsequent experiments using full-disk L1-level raw data with a spatial resolution of 4 km.

2.3. Quality control

Satellite IR radiance can barely penetrate clouds and can only detect information above the top of the cloud. Moreover, fast radiative transfer models do not perform well in simulating the BT of IR channels in cloud-covered areas. Therefore, this study excluded pixels affected by clouds from AGRI L1-level radiance data and assimilated only the clear-sky radiance of the AGRI. Cloud detection was performed using the 4-km resolution L2-level Cloud Mask product (CLM; Min et al., 2017; Wang et al., 2019) released by the

Table 1. Specifications for AGRI on board FY-4A.

Spectral coverage	Channel number	Spectral band (μm)	Spatial resolution (km)	Main application
VIS/NIR	1	0.45–0.49	1	Aerosol, visibility
	2	0.55–0.75	0.5	Fog, clouds
	3	0.75–0.90	1	Aerosol, vegetation
	4	1.36–1.39	2	Cirrus
	5	1.58–1.64	2	Cloud, snow
	6	2.10–2.35	2	Cloud phase, aerosol, vegetation
	7	3.50–4.00	2	Clouds, fire, moisture, snow
	8	3.50–4.00	4	Land surface
Midwave IR	9	5.8–6.7	4	Upper-level Water Vapor
	10	6.9–7.3	4	Midlevel Water Vapor
Longwave IR	11	8.0–9.0	4	Volcanic ash, cloud-top phase
	12	10.3–11.3	4	SST, LST
	13	11.5–12.5	4	Clouds, low-level WV
	14	13.2–13.8	4	Clouds, air temperature

National Satellite Meteorological Center [<http://satellite.nsmc.org.cn> (2021-08-17)]. CLM products include a four-level (confidently clear, probably clear, probably cloudy, and confidently cloudy) product, with only “confidently clear” pixels being assimilated (Fig. 2a). Additionally, only satellite zenith angles less than 60° were selected, due to the more serious deformation of the pixels with larger satellite zenith angle, and since high horizontal resolu-

tion of AGRI radiance data will lead to high computational cost and high correlation of observation errors. To avoid the above problems, the 20 km thinning mesh was used to select the observation data, which is approximately 3–6 times the horizontal resolution of WRF model used in this study (introduced in section 3.2) to avoid model noise.

Furthermore, to reduce systematic error in the data, additional quality control (QC) of the AGRI was performed during

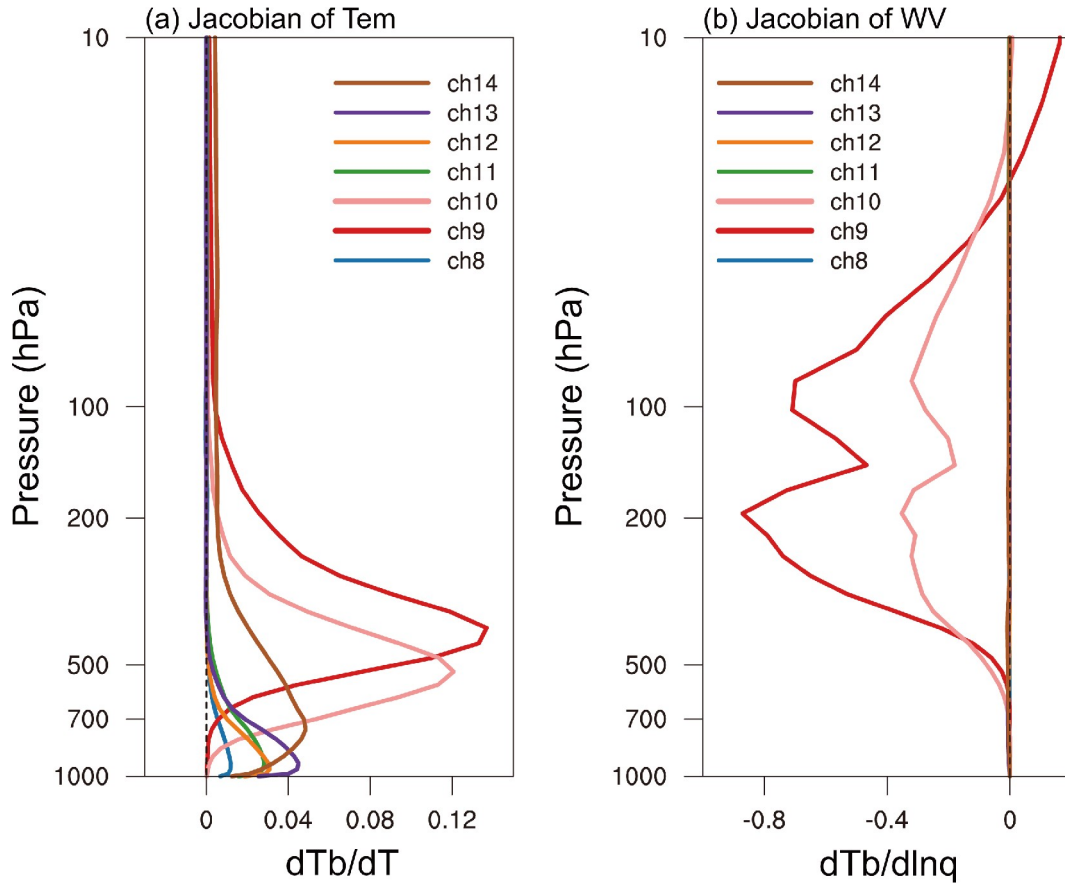


Fig. 1. Jacobian functions of (a) temperature and (b) WV of ch8-ch14 AGRI IR channels calculated by RTTOV.

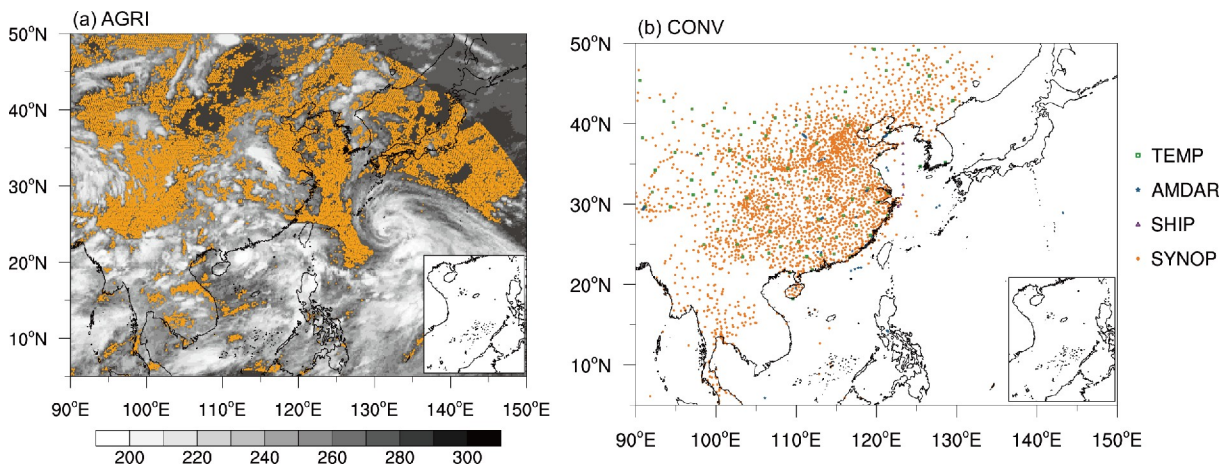


Fig. 2. The horizontal distribution of (a) observed BT (K) of ch13 (white-grey-black shading) and confidently clear pixels (orange dots) and (b) assimilated conventional observations at 1200 UTC 19 July 2021.

assimilation. The following pixels were removed from the AGRI data before minimization in WRFDA: (1) innovations (observed BT minus simulated BT) exceeding 1.5 K, which is slightly larger than the statistical bias of observation-minus-background (OMB) BT over two months; (2) innovations exceeding 3 times the standard deviation of observation error; and (3) cloud liquid water paths exceeding 0.05 kg m^{-2} , to assure that the pixels are clear-sky in the background as well. The quality of AGRI data was improved because of this QC. Figures 3a–d shows the distribution of OMB of the AGRI clear-sky radiance before and after bias correction, and the pixels covered by gray shading are assimilated after QC. It can be seen from the probability density function (PDF) that, after bias correction, the bias value for ch9

(ch10) clear-sky radiance is 0.37 (0.01), while the bias value calculated without Varbc is 0.75 (0.71). Ultimately, the pixels of ch9 and ch10 used for assimilation are colorful dots in Figs. 4e–f. It is worth noting that the number of observations that are used for assimilation also increased slightly after the bias correction. The observation error is slightly larger than the standard deviation statistics of one month's simulation deviations, and 1.2 K for both ch9 and ch10.

3. Case description and experimental setup

3.1. "21-7" Henan extremely heavy rainfall

From 17 to 22 July 2021, extremely heavy precipitation

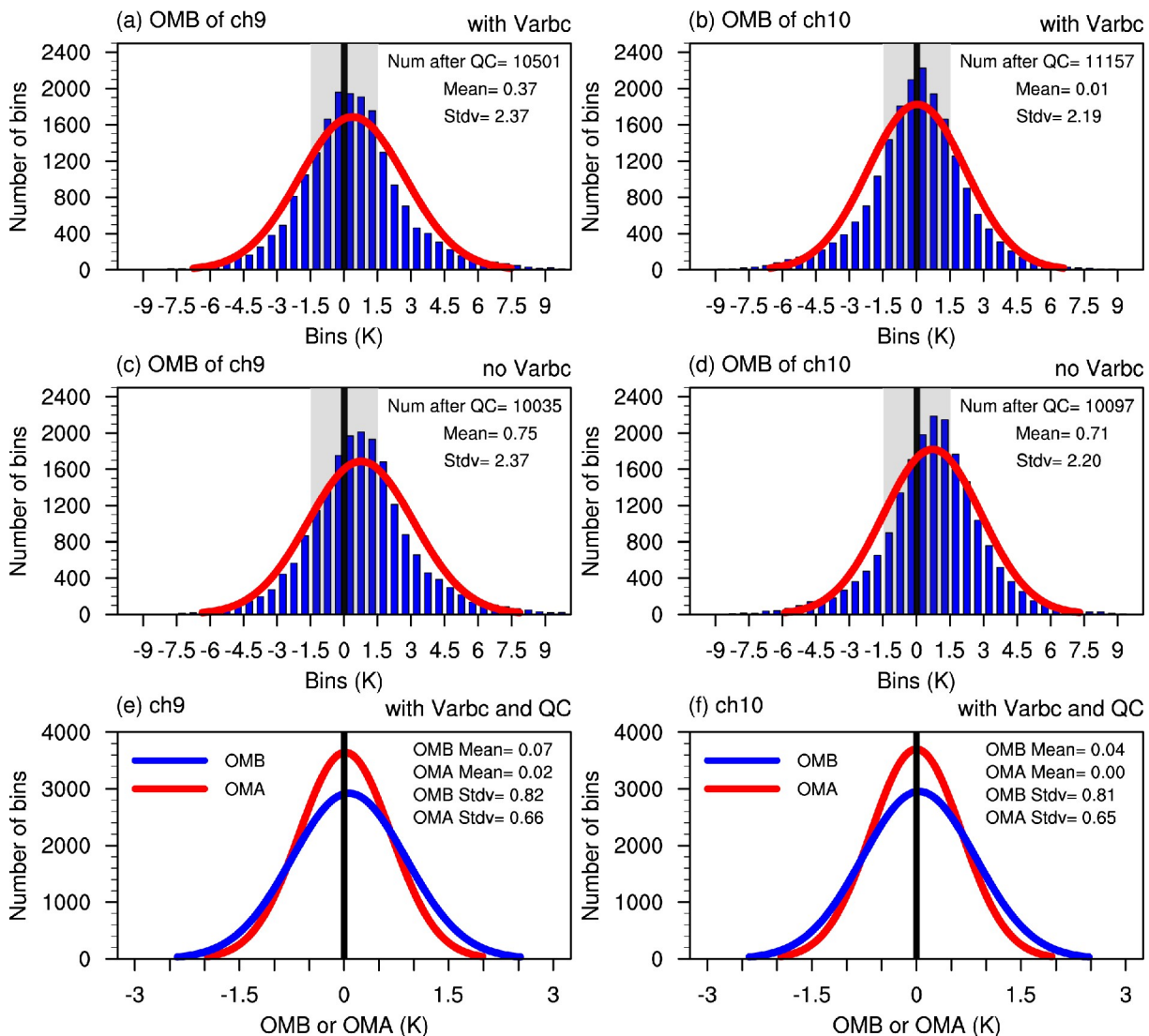


Fig. 3. Probability density function (PDF) of observation-minus-background (OMB, innovation) (a)–(b) with and (c)–(d) without Varbc for the AGRI observations of (a), (c) ch9; (b), (d) ch10, respectively, while the PDF of both the OMB and the Observation Minus Analysis (OMA) using Varbc and QC are shown for ch9 in (e) and ch10 in (f). The gray shading covers the pixels left after QC, whose count is represented by the “Num after QC”. The “Mean” and “Stdv” in (a)–(d) represent mean and standard deviations of all samples before QC. The “Mean” and “Stdv” in (e)–(f) represent mean and standard deviations of samples after QC. Black lines are the auxiliary line of 0. The samples are collected from the analysis at 1200 UTC 19 July.

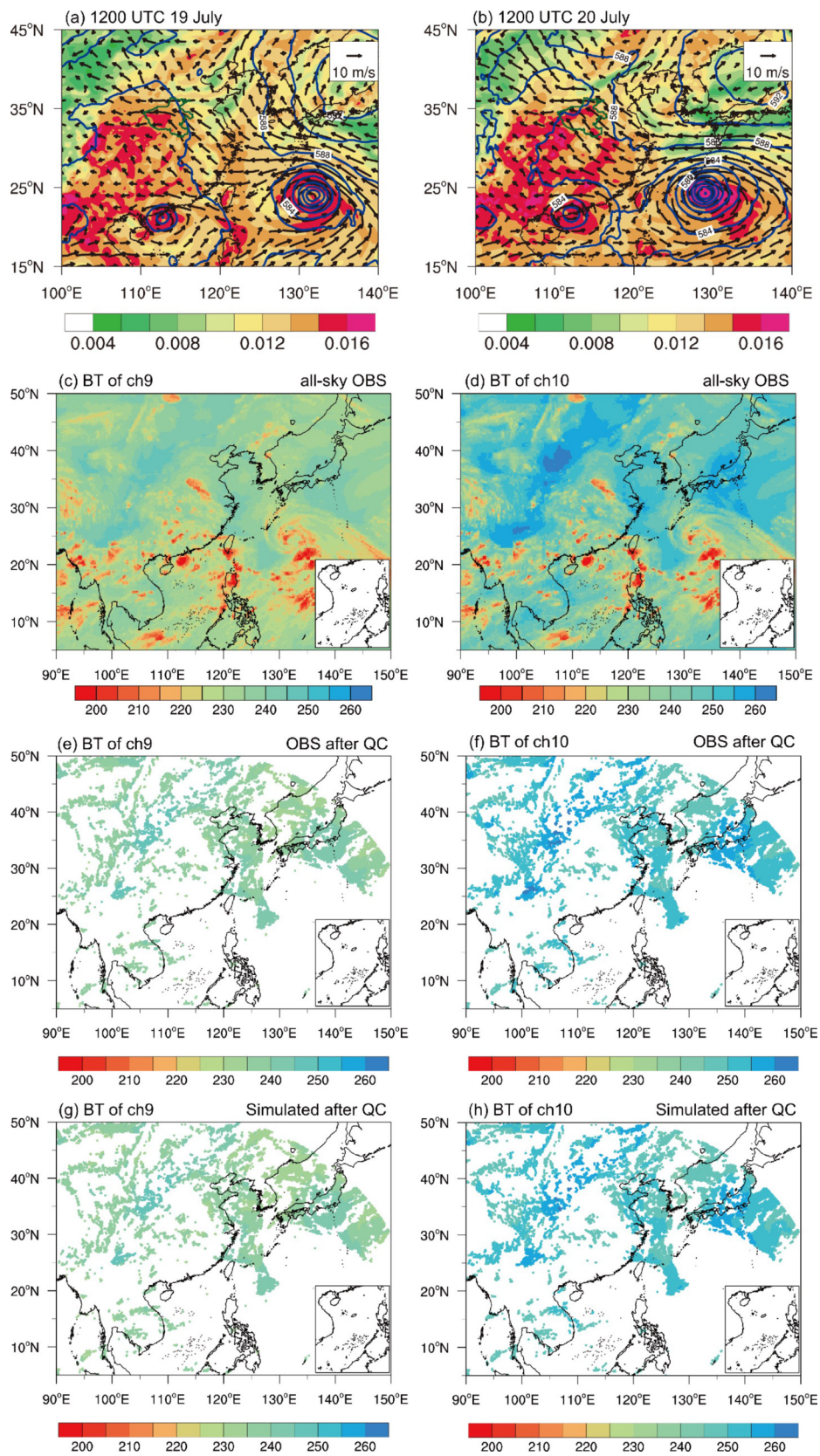


Fig. 4. Geopotential height (contours; gpm) at 500 hPa, specific humidity (shading; kg kg⁻¹) and wind (vectors; m s⁻¹) at 850 hPa of the ERA5 reanalysis at (a) 1200 UTC 19 July 2021; (b) 1200 UTC 20 July 2021. The all-sky observed BT (K) before QC are shown for ch9 in (c) and ch10 in (d), and the observed and simulated BT (K) after QC of (e, g) ch9 and (f, h) ch10 at 1200 UTC 19 July 2021.

occurred in Henan Province. On 20 July, Zhengzhou (capital of Henan Province) experienced a total of 201.9 mm of rainfall in only one hour, which broke the record for hourly precipitation on land in China. This event caused significant casualties and large economic losses (known as the “21·7” Henan extremely heavy rainfall).

The atmospheric circulation in the middle-to-lower troposphere is first analyzed using ERA5 reanalysis data (Hersbach et al., 2020) from 1200 UTC 19 July 2021 to 1200 UTC 20 July 2021 (Figs. 4a–b). Figures 4a–b shows that Henan Province was located between the strong western Pacific subtropical high pressure and continental high pressure, as well as the western Pacific tropical cyclone (TC) “In-fa” and the South China Sea TC “Cempaka”. Abundant WV from the Bay of Bengal and western Pacific Ocean was transported inland as the intense pressure gradient between TC “In-fa” and the subtropical high pressure strengthened the easterly winds, while the southeasterly jet on the southwestern side of the subtropical high pressure transported sufficient WV to Henan Province. This circulation situation was conducive to the formation of the severe rainstorm.

Figures 4c–d shows the all-sky observed BT of ch9 and ch10 before QC, and Figs. 4e–h shows the observed BT and simulated BT after QC of ch9 and ch10 (including cloud detection) at 1200 UTC 19 July 2021, respectively. The all-sky observed BT clearly shows the structure of TC “In-fa” and TC “Cempaka”, which coincides with atmospheric circulation of ERA5. After QC, only the pixels around the western Pacific subtropical high pressure and continental high pressure are left in ch9 and ch10 (Figs. 4e–h). The simulated BT (Figs. 4g–h) after QC is basically consistent with the observed BT distribution (Figs. 4e–f). Although the pixels reflecting the storm structure are rejected after QC, the airflow outside the storm is also important for prediction, especially in the “21·7” Henan extremely heavy rainfall, where the western Pacific subtropical high pressure and continental high pressure are very important influence systems.

3.2. Model configurations and experimental design

The simulated area for this study is depicted in Fig. 5. Centered at 28°N, 115°E, there are two nested domains, with 700×600 (lon. \times lat.) grid points (9 km) for domain 1 (d01) and 631×511 (lon. \times lat.) grid points (3 km) for domain 2 (d02), with 51 vertical levels and a model top of 50 hPa. The physical parameterizations are as follows: New Thompson microphysics scheme (Thompson et al., 2004), the Rapid Radiative Transfer Model for GCMs (RRTMG) longwave and shortwave radiance schemes (Iacono et al., 2000, 2004; Clough et al., 2005), Yonsei University planetary boundary layer scheme (Hong and Lim, 2006), Noah Land Surface Model (Tewari et al., 2004), New Tiedtke scheme cumulus scheme (Tiedtke, 1989) for d01, but with the cumulus parameterization for d02 switched off. This set of physical parameterizations is consistent with that used by the Beijing Meteorological Bureau, which is more conducive to the future application of AGRI DA in practical weather forecasting.

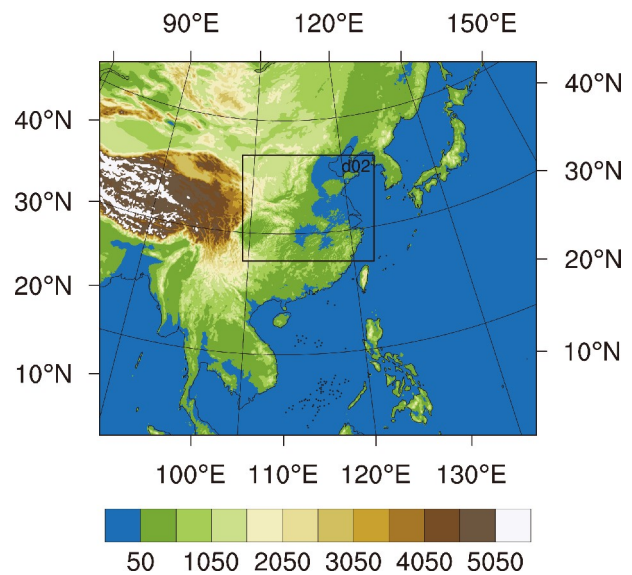


Fig. 5. Simulated area in ARW-WRF, the area shown in the figure is d01, and the area outlined by black line is d02.

The period chosen for the study in this paper is from 1200 UTC 19 July 2021 to 0000 UTC 21 July 2021. According to the hourly precipitation data from the national meteorological station, there were two extremely strong hourly precipitation events during this period, namely, from 0900 UTC to 1000 UTC on 20 July 2021 when the hourly precipitation in Zhengzhou reached 209.1 mm, and from 1400 UTC to 1500 UTC on 20 July 2021 when the hourly precipitation in Kaifeng reached 103.4 mm. Moreover, a maximum value of 24-h cumulative precipitation reached 532.6 mm from 1200 UTC 19 July to 1200 UTC 20 July.

With reference to the operational assimilation system, the partial cycle assimilation is carried out twice a day. Each partial cycle forecast 6 hours in advance as spin-up before it starts. That is, the partial cycle starting at 1200 UTC is assimilated at 0600 UTC and then integrated to 1200 UTC, and the second assimilation is carried out at 1200 UTC. At the same time, considering the timeliness of the global analysis field obtained in real time, the NCEP GFS [horizontal resolution of GFS data is $0.25^\circ \times 0.25^\circ$; <https://rda.ucar.edu/data/ds084.1/> (2021-09-12)] analysis field at 0600 UTC is used as the initial field for the regional model, and the boundary of the regional model is provided by the GFS forecast from 0600 UTC.

The partial cycle assimilation from 1200 UTC 19 July is used in this study according to precipitation duration and the period that extreme hourly precipitation occurred. Therefore, a 6-h spin-up run is first conducted as a cold-start from 0600 UTC 19 July to 1200 UTC 19 July, and DA is also conducted at 0600 UTC 19 July. Then, the second DA process is initialized at 1200 UTC 19 July using the 6-h forecast of cold-start as a background. Finally, a forecast of 36 hours is performed. Three parallel experiments are designed to evaluate the effect of the AGRI on the “21·7” Henan extremely heavy rainfall. The first experiment (hereafter “CTRL”) is

a 6-h spin-up and 36-h forecast from 0600 UTC 19 July without DA, only using the GFS forecast as the background and lateral boundary conditions. The second experiment (hereafter “CONV”) is similar to the first, except that it assimilates conventional observations including radiosondes, ships, surface synoptic observations, and airport reports (Fig. 2b), with the conventional observations within 3-h window before and after the analysis time being used. The third experiment (hereafter “AGRI + CONV”) assimilates the same conventional observations as the “CONV” experiment, as well as clear-sky AGRI radiance from two WV channels (Fig. 4e–f). However, different from the time window of conventional observations, only the AGRI clear-sky radiance at the analysis time is assimilated because the temporal resolution of the AGRI data is so high. The assimilation is performed in both domains, d01 and d02, and the background error covariance of the NCEP CV3 global climate state is used in this study.

4. Results

4.1. Analysis increment

In Figs. 3e and 3f above, the PDF of OMB and OMA statistics for ch9 and ch10 were shown. It can be seen that the mean value of ch9 (ch10) of OMA after assimilation is 0.02 (0.0) and the standard deviation is 0.66 (0.65), which are less than the mean value of OMB of 0.07 (0.04) and the standard deviation of 0.82 (0.81) after QC calculated by pixels covered by gray shading in Figs. 3a and 3b. Both the mean value and standard deviation of OMA are smaller than OMB, indicating that the DA of AGRI WV channels radiance is correct in this study.

Analysis increments for the two assimilation experiments are shown in Fig. 6. There are differences in the analysis increments after assimilation in both of the two experiments CONV and AGRI+CONV. Although the patterns of water vapor flux (WVF) and wind increments at 850 hPa in the

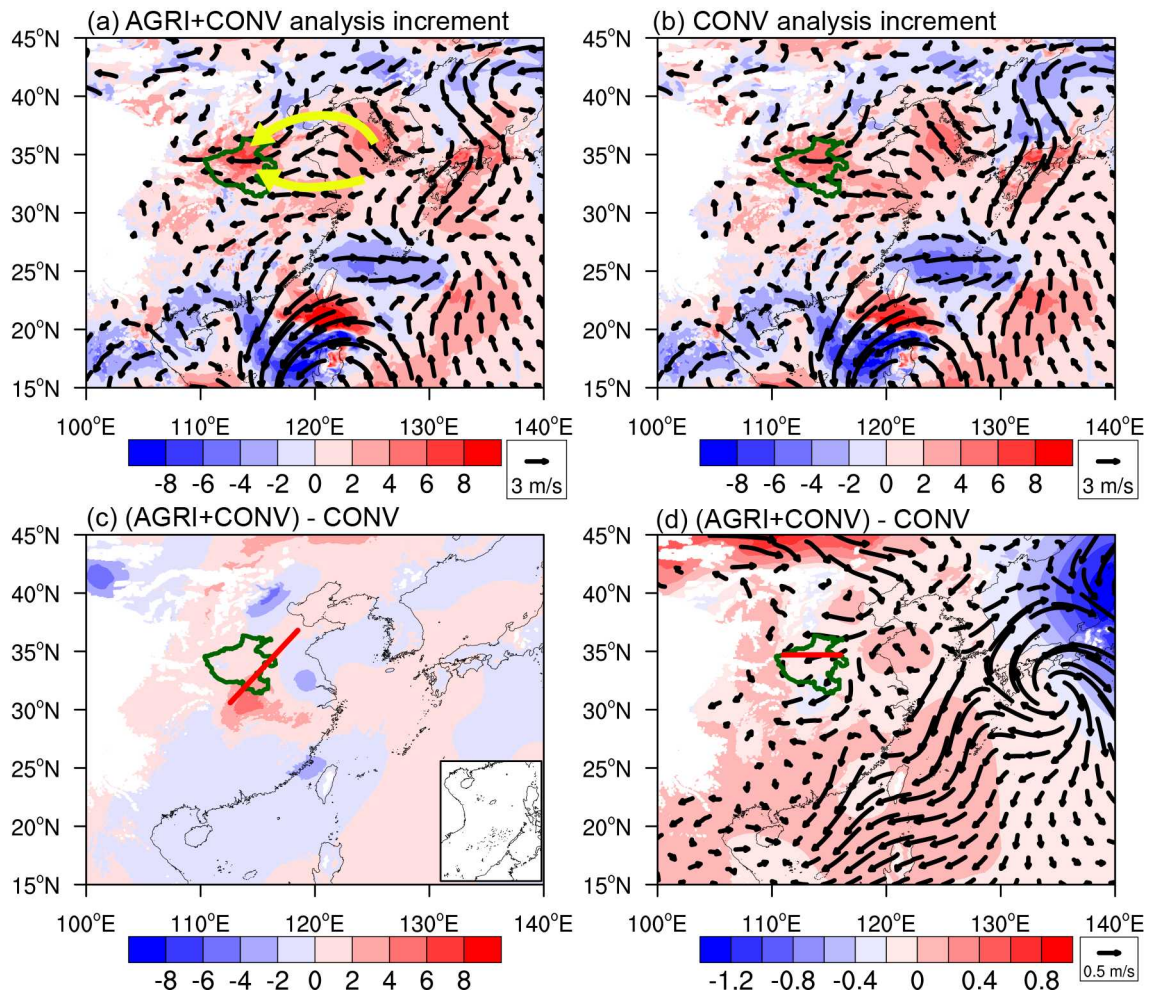


Fig. 6. WVF value (shading; $10^{-2} \text{ g cm}^{-1} \text{ hPa}^{-1} \text{ s}^{-1}$) and wind (vector; m s^{-1}) increment at 850 hPa in the (a) AGRI+CONV and (b) CONV experiments, and difference of (c) specific humidity increment ($10^{-4} \text{ kg kg}^{-1}$) and (d) wind increment (vector; m s^{-1}) and temperature increment (K) at 850 hPa between the AGRI+CONV and CONV experiments [(AGRI+CONV)–CONV] at 1200 UTC 19 July 2021. The yellow lines in (a) represent the two enhanced water vapor transport paths. The red lines in (c) and (d) show the locations of the cross sections appearing in Fig. 10.

two assimilation experiments are similar (Figs. 6a and 6b), the WVF over northern Henan are stronger in the AGRI+CONV experiment than that in the CONV experiments. The DA results in two enhanced WV transport paths in both the CONV and AGRI+CONV experiments compared with the CTRL experiment (shown by the yellow marked lines in Fig. 6a). The differences in specific humidity, temperature and wind increment at 850 hPa between the AGRI+CONV and CONV experiments, are shown in Fig. 6c and 6d, respectively. In the AGRI+CONV experiment, the value of the specific humidity increment is larger in southeastern Henan than in the CONV experiment (Fig. 6c), and similar features are found in the lower troposphere (not shown). Furthermore, Fig. 6d shows that the main difference between the AGRI+CONV experiment and the CONV experiment is over the ocean, due to the additional ocean observations provided by FY-4A AGRI (Fig. 2a), which compensate for the lack of ocean observations. A significant negative analysis increment of temperature is seen in the AGRI+CONV experiment over the Sea of Japan, whereas this negative analysis increment is not evident in the CONV experiments (Fig. 6d), precisely because of the role of satellite information in this region, which first adjusts the atmospheric temperature and

humidity fields and thus the wind fields over the ocean.

4.2. Rainfall forecast

Precipitation forecasts are a comprehensive element in assessing the effects of assimilation. Figure 7 shows the 24-h accumulated precipitation from observations (Fig. 7a) and three experiments (Figs. 7b–d) initialized at 1200 UTC 19 July 2021. The observed rainfall is taken from 121 national meteorological stations in Henan Province. The spatial distribution of observed rainfall shows a large maximum in Zhengzhou, with precipitation above 250 mm distributed in a west-east zonal band, and the most intense rainfall reaching 532.6 mm located at 34.71°N, 113.66°E (Fig. 7a). However, in the CTRL experiment, the rainfall over 250 mm is relatively scattered, with a simulated maximum precipitation of 376.6 mm (Fig. 7b), which is much less than the observed value. The CONV experiment simulates a band of precipitation above 250 mm, similar to the observations, but the center of precipitation is southeastward relative to the observation, with a simulated maximum rainfall intensity of 401.9 mm. There is an improvement over the CTRL experiment but still lower than that of the observed value (Fig. 7c). In contrast, the distribution of precipitation above 250 mm in the

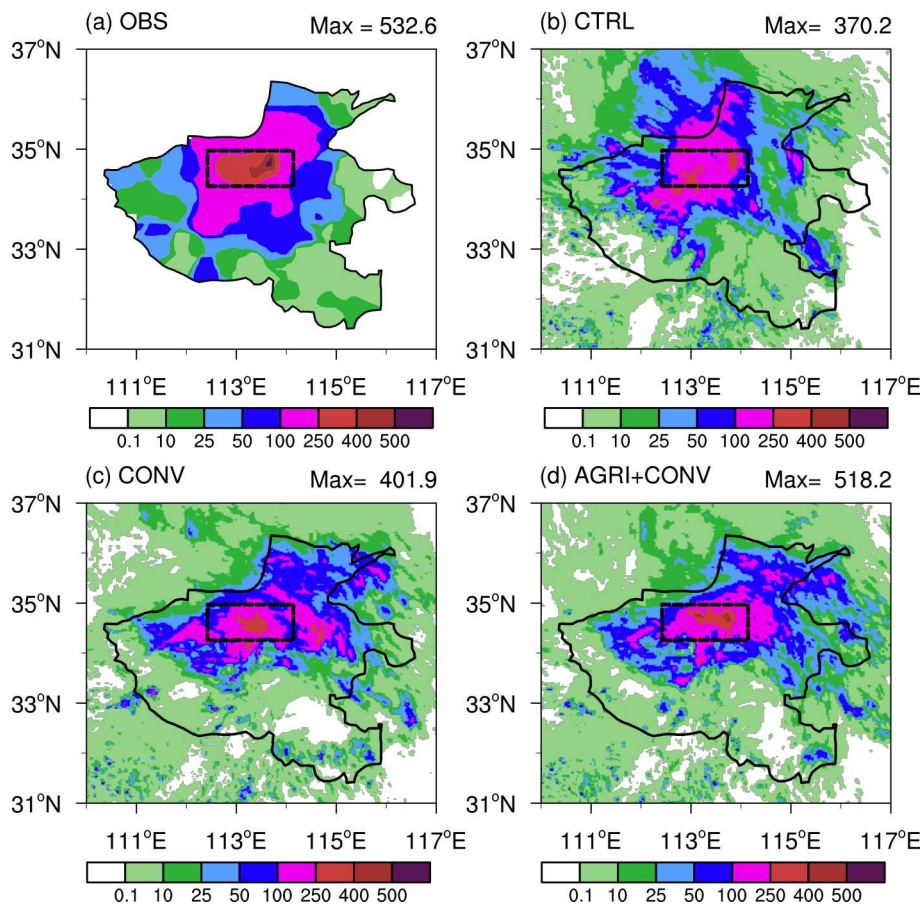


Fig. 7. (a) The observed 24-h accumulated rainfall (shading; mm) and the corresponding forecast rainfall (shading; mm) from the (b) CTRL, (c) CONV and (d) AGRI + CONV experiments from 1200 UTC 19 July 2021 to 1200 UTC 20 July 2021. The black box represents the Zhengzhou area.

AGRI+CONV experiment agrees better with the observations. Moreover, the simulated maximum rainfall intensity in the AGRI+CONV experiment reaches 518.2 mm, which exceeds the value in the CONV experiment and is approximately comparable to the observed value (Fig. 7d). The results indicate that simulated 24-h accumulated precipitation in the AGRI+CONV experiment is improved in terms of the location and intensity compared with the CTRL and CONV experiments.

In addition to the 24-h accumulated precipitation, short periods of intense precipitation processes are also important. The daily variation in 3-h accumulated precipitation is analyzed, and it is found that the forecast of the daily trend of 3-h accumulated precipitation during this process is 4 hours ahead of the observed trend. The distribution of 3-h cumulative precipitation during the two hourly heavy precipitation events is given. Figures 8a–d shows the 3-h accumulated precipitation for observations (Fig. 8a) from 0900 UTC to 1200 UTC 20 July 2021 and for the three experiments (Figs. 8b–d) from 0500 UTC to 0800 UTC 20 July 2021. Figure 8e is the same as Fig. 8a but from 1300 UTC 20 to 1600 UTC 20 July 2021, and Figs. 8f–h is the same as Fig. 8b–d but from 0900 UTC 20 to 1200 UTC 20 July 2021. The simulation of the two periods shown in Fig. 8 is four hours ahead of the observed time. Figure 8a shows that Zhengzhou station (34.71°N, 113.66°E) received the greatest amount of rainfall at 278.9 mm. Whereas most other stations outside Zhengzhou generally received less than 25 mm of rainfall, this extreme 3-h cumulative precipitation was entirely localized, which greatly increases the challenges of NWP. In the CTRL experiment, the precipitation center is to the northwest and much less intense than the observed center (Fig. 8b). The assimilation results of the CONV experiment show three precipitation centers located to the west and southwest of the observations, while the AGRI+CONV experiment pinpointed the precipitation center. The maximum rainfall in the CONV experiment is higher than that in the CTRL experiment but still much lower than the observation. Although the AGRI+CONV experiment also underestimates the maximum rainfall intensity, the AGRI+CONV experiment is closer to observations than the other two experiments.

Although the rainfall from 1300 UTC to 1600 UTC 20 July 2021 was also intense (Fig. 8e), the rainfall region was much larger than that shown in Fig. 8a. The 3-h accumulated precipitation had two centers located at Kaifeng and Zhoukou, with the most intense rainfall reaching 157 mm at Kaifeng station (34.8°N, 114.29°E) (Fig. 8e). The CTRL experiment simulates only one precipitation center located to the west of Kaifeng and misses the center near Zhoukou (Fig. 8f). The CONV experiment simulates three precipitation centers, with only the northern center being more consistent with the observed area yet smaller in extent (Fig. 8g). The AGRI+CONV experiment simulates two precipitation centers, which is more consistent with the observed locations, but with a smaller coverage than the observations (Fig. 8h). The maximum precipitation simulated for all three experiments is higher than that observed. For several complex rea-

sons, such as resolution or physical processes, there may be biases in the numerical model of intense precipitation. Nevertheless, it is worth emphasizing that the assimilation of AGRI radiance helps to adjust the location and intensity of precipitation.

4.3. Analysis of the impact on rainfall forecast

To investigate the impact of AGRI assimilation on rainfall forecasts, the analysis and forecast fields after assimilation for both the CONV and AGRI+CONV experiments are shown Fig. 9, respectively. As shown by the two brown arrows in Fig. 9a, two WV transport paths can be seen in the analysis fields of both experiments; the first from the Yellow Sea northwards through the Shandong Peninsula and then turning southwards to enter from northern Henan, and the second passing through Anhui Province and coming in from southeastern Henan under easterly-southeasterly flow. The second WV transport path is wider and stronger due to the stronger and more westerly subtropical high pressure, as seen in Figs. 9a and 9e, where the 588 gpm geopotential height contour extends inland in eastern China.

At 1200 UTC 19 July 2021, the southeasterly flow crossed the Dabie Mountains and transported WV to the entire Henan region (Figs. 9a and 9e). However, the differences in the analysis increments after assimilation in the AGRI+CONV and CONV experiments (Fig. 6) lead to different trends in the forecasts of the circulation field. Subsequent forecasts show that in the AGRI+CONV experiment (Figs. 9b–d), the subtropical high pressure has weakened and retreated to the northeast, and the 588 gpm geopotential height contour has retreated to the sea, which has caused the southeasterly flow to contract to the northeast. However, the retreat of the 588 gpm contour in the CONV experiment is not as obvious, and even at 0500 UTC on 20 July, it still extends westward inland (Figs. 9f–h). The difference in the location of the subtropical high pressure between the AGRI+CONV and CONV experiments is clearly shown by contours in Figs. 9i–l. Additionally, with the retreat of the subtropical high pressure and weaker southeasterly flow, the WV transport path from the northwestern Pacific to Henan narrows and contracts to the north of the Dabie Mountains in the AGRI+CONV experiment (Figs. 9c–d), though some WV can still cross the Dabie Mountains into Henan in the CONV experiment (Figs. 9g–h). Ultimately, the difference of WVF is positive (negative) (Fig. 9l), implying there is greater WVF at (west of) Zhengzhou station in the AGRI+CONV (CONV) experiment. As a result, the AGRI+CONV experiment pinpoints the precipitation center, while the precipitation centers are located to the west and southwest of the observations in the CONV experiment (Figs. 8c–d). This phenomenon can also be seen in the vertical profile distribution of WVF (Fig. 10).

Vertical cross sections along the red line in Fig. 6c (Fig. 6d) are shown in Figs. 10a–d and Figs. 10f–i (Figs. 10e and j) to study the variation in simulated humidity and wind field from 1200 UTC 19 July to 1200 UTC 20 July 2021. At the analysis time (1200 UTC 19 July), the WV band entering

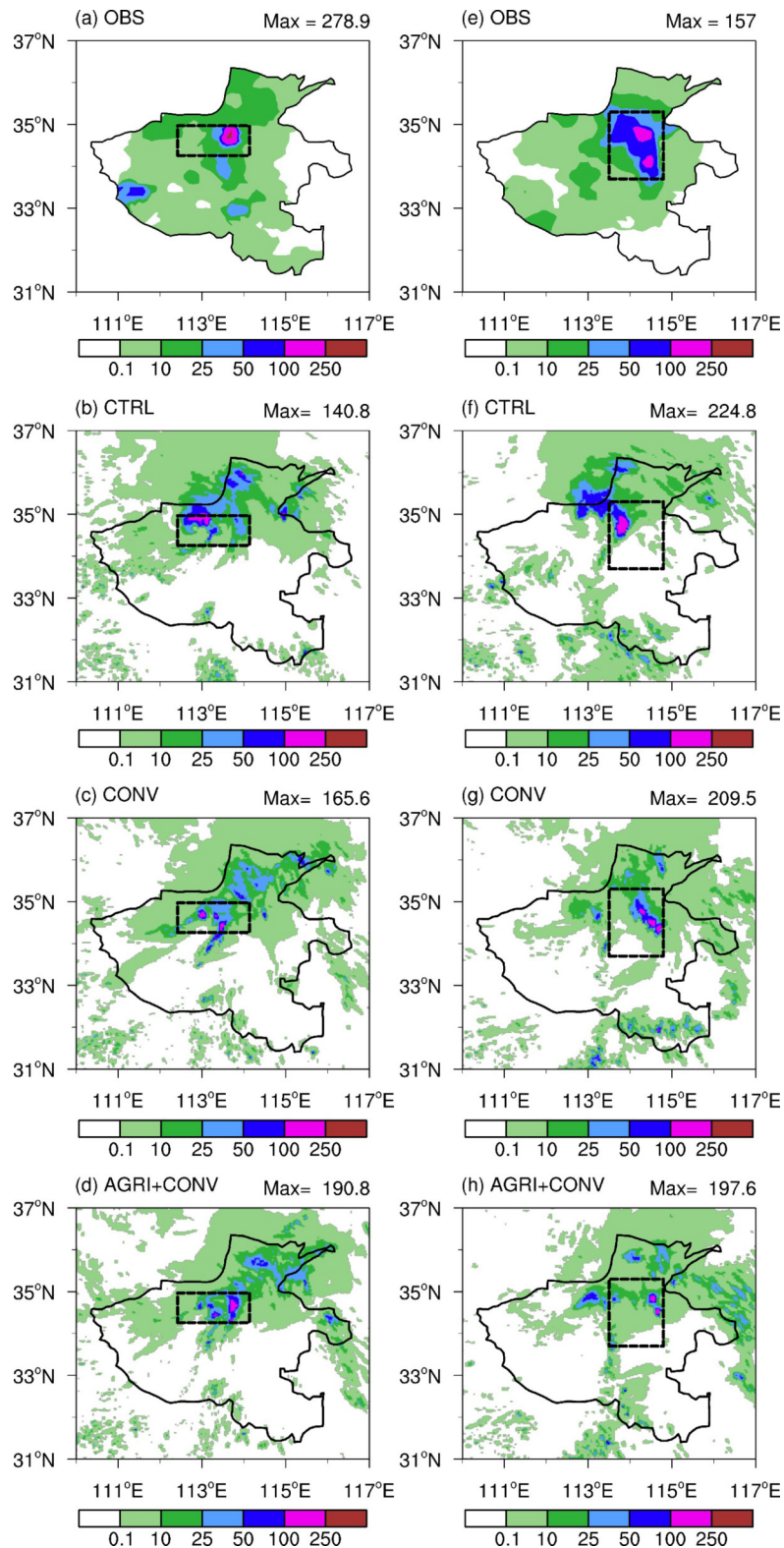


Fig. 8. (a) The observed 3-h accumulated rainfall (shading; mm) from 0900 UTC 20 to 1200 UTC 20 July 2021 and the corresponding forecast rainfall (shading; mm) from the (b) CTRL, (c) CONV and (d) AGRI + CONV experiments from 0500 UTC 20 to 0800 UTC 20 July 2021. Panel (e) is the same as (a), but from 1300 UTC 20 to 1600 UTC 20 July 2021 and (f)–(h) is the same with (b)–(d), but from 0900 UTC 20 to 1200 UTC 20 July 2021. The black boxes in (a)–(d) represent the Zhengzhou and in (e)–(h) represent the Kaifeng and Zhoukou areas.

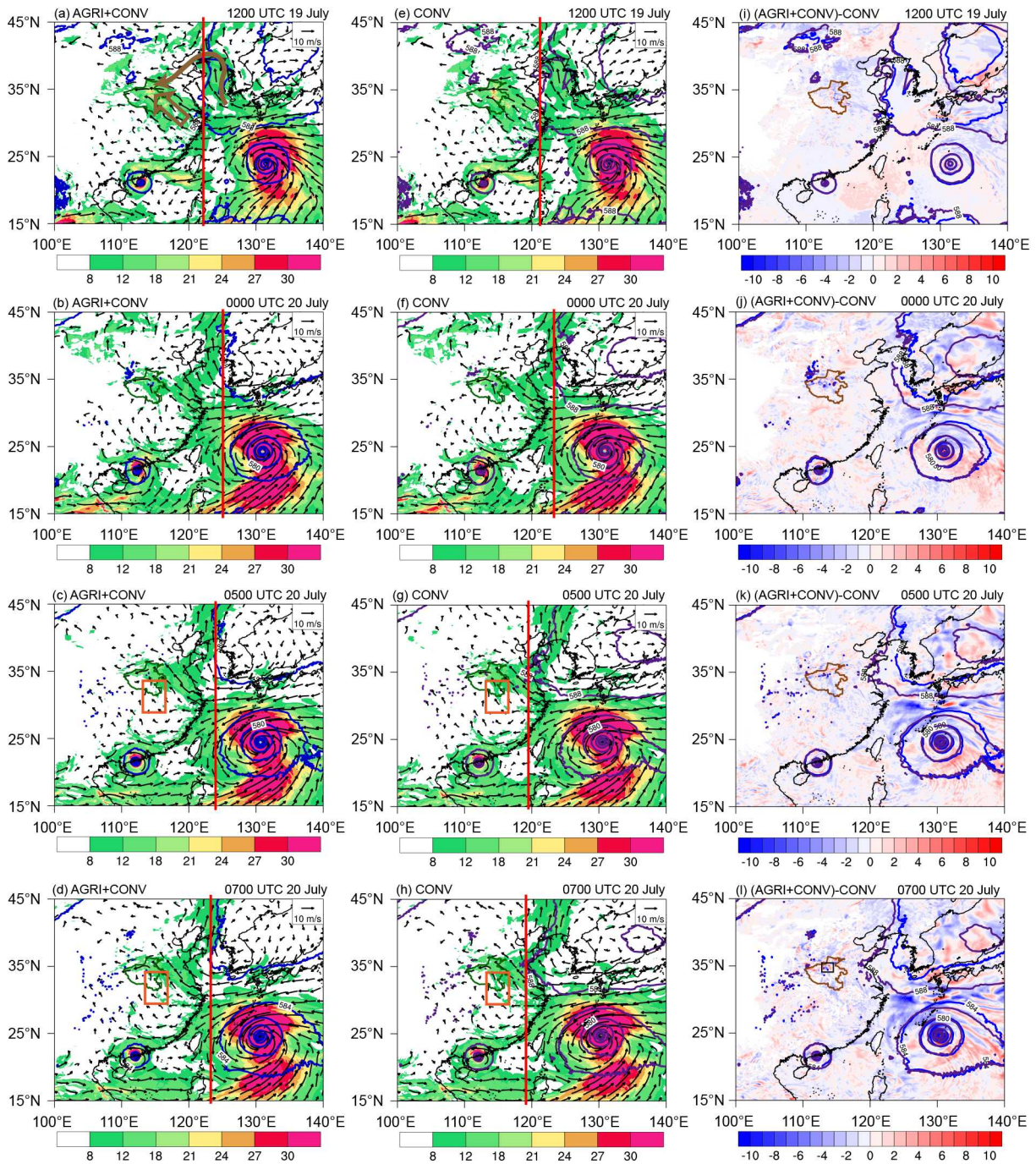


Fig. 9. Geopotential height (contours; gpm) at 500 hPa and WVf value (shading; $10^{-2} \text{ g cm}^{-1} \text{ hPa}^{-1} \text{ s}^{-1}$), wind (vectors; m s^{-1}) at 850 hPa in the AGRI+CONV experiment at (a) 1200 UTC 19 July 2021; (b) 0000 UTC 20 July 2021; (c) 0500 UTC 20 July 2021; (d) 0700 UTC 21 July 2021. Panels (e)–(h) are the same as (a)–(d), but for the CONV experiment. (i)–(l) Geopotential height (contours; units: gpm) at 500 hPa in the AGRI+CONV (blue contours) and CONV (purple contours) experiments and WVf (shading; units: $10^{-2} \text{ g cm}^{-1} \text{ hPa}^{-1} \text{ s}^{-1}$) of [(AGRI+CONV) - CONV] at 850 hPa. The brown arrows in (a) represent the two water vapor transport paths. The red auxiliary lines represent the western edge of the subtropical ridge. The orange boxes in (c)–(d) and (g)–(h) represent the areas around the Dabie Mountains, and the black box in (l) represent the areas around Zhengzhou station.

Henan is relatively wide in the lower troposphere (Figs. 10a and 10f), and then narrows and propagates northeastwards (Figs. 10b and 10g), which could explain why the precipitation covers southwestern Henan during 1200–1800 UTC 19 July, and then the precipitation center gradually moves north-

eastward to Zhengzhou (not shown). This is consistent with the assimilation leading to the retreat of subtropical high pressure to the northeast in Fig. 9. By comparing the WVf value of the AGRI+CONV and CONV experiments in Fig. 10, it can be seen that the WVf value over $20 \text{ g cm}^{-1} \text{ hPa}^{-1} \text{ s}^{-1}$

reached a higher level at approximately 33.5°N in the AGRI+ CONV experiment at 1200 UTC 19 July (Fig. 10a), while in the CONV experiment such large values of WVf are only below 850 hPa (Fig. 10f). It can also be seen in the subsequent forecasts that the WVf is more concentrated (Figs. 10c–d) than that in the CONV experiment (Figs. 10h–i) due to the more concentrated wind distribution in the lower troposphere

along the cross section. Specifically, wind speeds above 8 m s⁻¹ extended to the surface layer in the AGRI+CONV experiment, while they are distributed above 900 hPa in the CONV experiment. As a result, there is high WV transport in a relatively narrow band in the lower troposphere in the AGRI+CONV experiment at 0700 UTC 20 July 2021 (Fig. 10d), and the destination of this WV is the center of

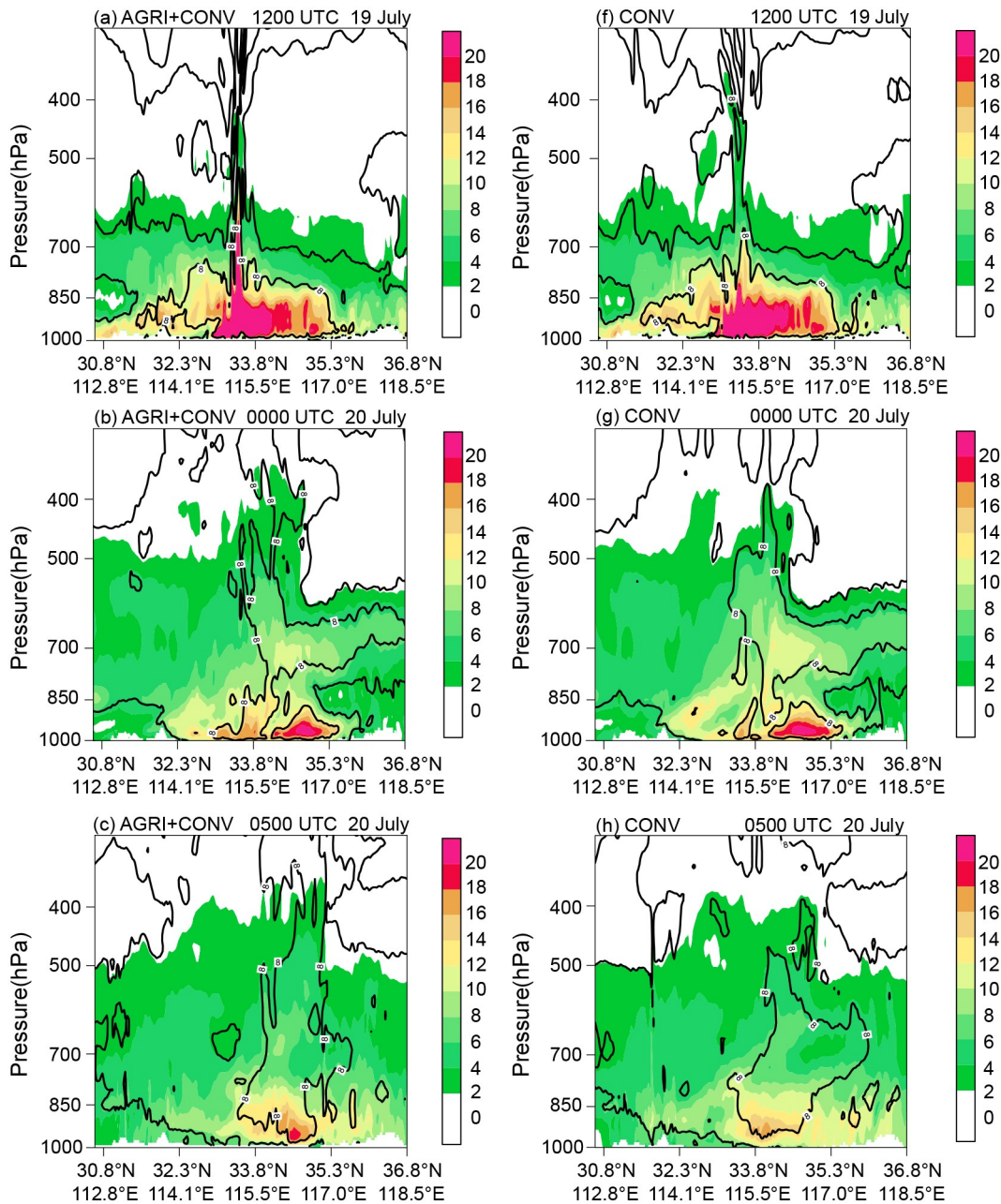


Fig. 10. The cross sections between (30.6°N, 112.6°E) and (36.8°N, 118.5°E) of WVf value (shading; 10⁻² g cm⁻¹ hPa⁻¹ s⁻¹) and wind speed (contours; m s⁻¹) at (a) 1200 UTC 19 July 2021, (b) 0000 UTC 20 July 2021, (c) 0500 UTC 20 July 2021 and (d) 0700 UTC 20 July 2021 from the AGRI+CONV experiment. (f)–(i) are the same as (a)–(d), but for the CONV experiment. (e) Longitude–pressure cross sections of water vapor flux divergence (shading; 10⁻² g cm⁻² hPa⁻¹ s⁻¹), zonal circulation (vectors; zonal wind, m s⁻¹; vertical motion, 10⁻¹ m s⁻¹), and zonal distribution of 1 h accumulated rainfall forecast (mm) along 34.76°N in the AGRI+CONV experiment at 0800 UTC 20 July 2021. Panel (j) is same as (e) but along 34.65°N in the CONV experiment.

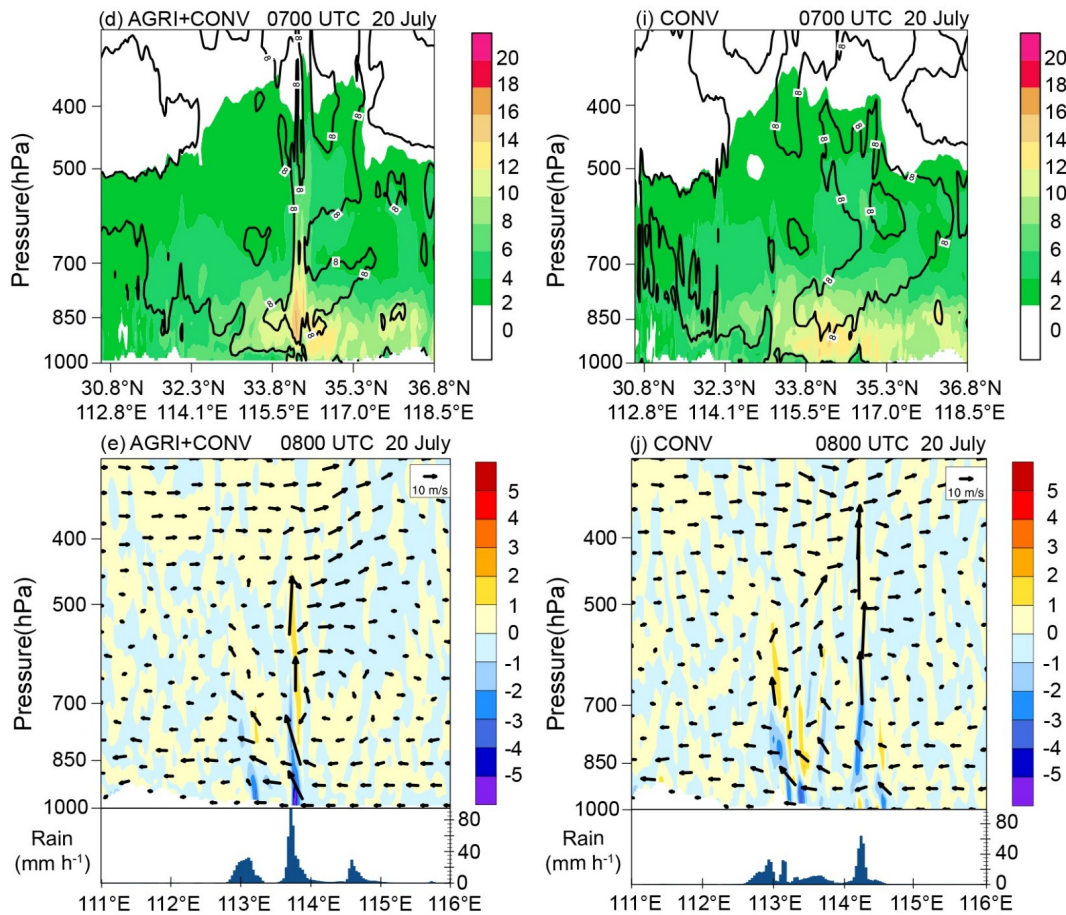


Fig. 10. (Continued).

the heavy precipitation center at Zhengzhou at 0800 UTC 20 July 2021 in the model simulation, corresponding to the large value area of WV convergence and upwelling in Fig. 10e. In contrast, the WV convergence and ascending motion in the CONV experiment are much more dispersed (Fig. 10j); therefore, the precipitation center of this experiment is also more dispersed and not concentrated at Zhengzhou (Fig. 8c).

5. Conclusion and discussion

In this study, the assimilation of the clear-sky radiance of the FY-4A AGRI WV channels in a regional high-resolution model is carried out, and the forecast effects of the assimilation of the two WV channels with conventional observations for the “21·7” Henan extremely heavy rainfall is analyzed, compared with a baseline experiment which only assimilated conventional observations. Assimilation is performed by WRFDA with the 3DVar method in a 9 km/3 km nested grid configuration. The 24-h accumulated precipitation from 1200 UTC 19 July to 1200 UTC 20 July 2021 forecasted in the AGRI+CONV experiment exceeded 500 mm, which is close to a maximum value of 532.6 measured at national meteorological stations; also, the location of the maximum rainfall is consistent with observations. Analysis of the 3-h cumula-

tive precipitation shows that the forecast of the daily trend of the 3-h cumulative precipitation during this process is 4 hours ahead of the observed trend. However, the simulation is more accurate for the location and intensity of the two heavy precipitation events that occurred in Zhengzhou, Kaifeng and Zhoukou.

The analysis increment shows that the main difference between the AGRI+CONV experiment and CONV experiment is over the ocean, due to the additional ocean observations provided by FY-4A, which compensate for the lack of ocean observations. In the AGRI+CONV experiment, there is a significant negative analysis increment in temperature over the Sea of Japan, which is not evident in the CONV experiment, precisely because of the role of satellite information in the region which adjusts the wind field over the ocean by adjusting the atmospheric temperature. This adjustment causes the subtropical high pressure to weaken and retreat to the northeast, while the southeastern flow also contracts with it to the northeast. Thus, as the subtropical high pressure retreats, the WV transport path from the Pacific Northwest to Henan narrows in the AGRI+CONV experiment, contracting to the north of the Dabie Mountains. However, the retreat of the 588 gpm geopotential height contour in the CONV experiment is not obvious, and some WV could still cross the Dabie Mountains into Henan. In addi-

tion, the stronger wind in the AGIR+CONV experiment extends to the surface layer, which results in a narrow and higher WV transport band in the lower troposphere, and the destination of this WV transport corresponds exactly to the center of heavy precipitation in Zhengzhou. In contrast, the convergence and upward movement of WV in the CONV experiment is more dispersed; therefore, the precipitation centers in this experiment are also more dispersed and not concentrated in Zhengzhou.

This study can provide a useful reference for using FY-4A data in regional models to improve storm forecasting. However, the current work is mainly focused on clear-sky radiance and there are still many challenges to be addressed to make the most effective use of AGRI all-sky radiances. Research that has been completed provides much valuable guidance (Bauer et al., 2011; Wang et al., 2015; Okamoto, 2017; Geer et al., 2019; Lee et al., 2019; Okamoto et al., 2019; Otkin and Potthast, 2019). It was found that all-sky radiance assimilation has clear advantages over clear-sky radiance assimilation (Okamoto et al., 2019). Therefore, AGRI all-sky radiance assimilation is worth studying in the future. In addition, Honda et al. (2018) further found the advantage of rapid 10-min DA of all-sky AHI WV radiance in a TC forecast. This also provides motivation for conducting high-frequency AGRI DA experiments and attempting to assimilate AGRI radiance with the 4DVar method (Bauer et al., 2010; Yin et al., 2021).

Acknowledgements. This study was supported by the National Key R&D Program of China (Grant Nos. 2017YFC1501803 and 2017YFC1502102). The authors appreciate Miss Ruoqing YAN for support of rainfall scripts.

REFERENCES

- Auligné, T., A. P. McNally, and D. P. Dee, 2007: Adaptive bias correction for satellite data in a numerical weather prediction system. *Quart. J. Roy. Meteor. Soc.*, **133**, 631–642, <https://doi.org/10.1002/qj.56>.
- Bauer, P., A. J. Geer, P. Lopez, and D. Salmond, 2010: Direct 4D-Var assimilation of all-sky radiances. Part I: Implementation. *Quart. J. Roy. Meteor. Soc.*, **136**(652), 1868–1885, <https://doi.org/10.1002/qj.659>.
- Bauer, P., and Coauthors, 2011: Satellite cloud and precipitation assimilation at operational NWP centres. *Quart. J. Roy. Meteor. Soc.*, **137**, 1934–1951, <https://doi.org/10.1002/qj.905>.
- Bessho, K., and Coauthors, 2016: An introduction to himawari-8/Y Japan's new-generation geostationary meteorological satellites. *J. Meteor. Soc. Japan*, **94**, 151–183, <https://doi.org/10.2151/jmsj.2016-009>.
- Charlton-Perez, C., H. L. Cloke, and A. Ghelli, 2015: Rainfall: High-resolution observation and prediction. *Meteorological Applications*, **22**, 1–2, <https://doi.org/10.1002/met.1496>.
- Cintineo, R. M., J. A. Otkin, T. A. Jones, S. Koch, and D. J. Stensrud, 2016: Assimilation of synthetic GOES-R ABI infrared brightness temperatures and WSR-88D radar observations in a high-resolution OSSE. *Mon. Wea. Rev.*, **144**, 3159–3180, <https://doi.org/10.1175/MWR-D-15-0366.1>.
- Clough, S. A., M. W. Shephard, E. J. Mlawer, J. S. Delamere, M. J. Iacono, K. Cady-Pereira, S. Boukabara, and P. D. Brown, 2005: Atmospheric radiative transfer modeling: A summary of the AER codes. *Journal of Quantitative Spectroscopy and Radiative Transfer*, **91**, 233–244, <https://doi.org/10.1016/j.jqsrt.2004.05.058>.
- Collard, A. D., 2007: Selection of IASI channels for use in numerical weather prediction. *Quart. J. Roy. Meteor. Soc.*, **133**(629), 1977–1991, <https://doi.org/10.1002/qj.178>.
- Collard, A. D., and A. P. McNally, 2009: The assimilation of Infrared Atmospheric Sounding Interferometer radiances at ECMWF. *Quart. J. Roy. Meteor. Soc.*, **135**(641), 1044–1058, <https://doi.org/10.1002/qj.410>.
- Dee, D. P., 2004: Variational bias correction of satellite radiance data in the ECMWF system. *Proc. ECMWF Workshop on Assimilation of High Spectral Resolution Sounders in NWP*, Reading, UK, 97–112.
- Dee, D. P., 2005: Bias and data assimilation. *Quart. J. Roy. Meteor. Soc.*, **131**, 3323–3343, <https://doi.org/10.1256/qj.05.137>.
- Di, D., Y. F. Ai, J. Li, W. J. Shi, and N. M. Lu, 2016: Geostationary satellite-based 6.7 μm band best water vapor information layer analysis over the Tibetan Plateau. *J. Geophys. Res.*, **121**(9), 4600–4613, <https://doi.org/10.1002/2016JD024867>.
- Eresmaa, R., J. Letertre-Danczak, C. Lupu, N. Bormann, and A. P. McNally, 2017: The assimilation of Cross-track Infrared Sounder radiances at ECMWF. *Quart. J. Roy. Meteor. Soc.*, **143**, 3177–3188, <https://doi.org/10.1002/qj.3171>.
- Eyre, J., 1991: A fast radiative transfer model for satellite sounding systems. ECMWF Tech. Memo. 176, 30 pp.
- Eyre, J., 1992: A bias correction scheme for simulated TOVS brightness temperatures. ECMWF Tech. Memo. 186, 34 pp.
- Geer, A. J., S. Migliorini, and M. Matricardi, 2019: All-sky assimilation of infrared radiances sensitive to mid- and upper-tropospheric moisture and cloud. *Atmospheric Measurement Techniques*, **12**, 4903–4929, <https://doi.org/10.5194/amt-12-4903-2019>.
- Geng X. W., J. Z. Min, C. Yang, Y. B. Wang, and D. M. Xu, 2020: Analysis of FY-4A AGRI bias characteristics and correction experiment. *Chinese Journal of Atmospheric Sciences*, **44**(4), 679–694, <https://doi.org/10.3878/j.issn.1006-9895.1907.18254>. (in Chinese with English abstract)
- Harris, B. A., and G. Kelly, 2001: A satellite radiance-bias correction scheme for data assimilation. *Quart. J. Roy. Meteor. Soc.*, **127**(574), 1453–1468, <https://doi.org/10.1002/qj.49712757418>.
- Hersbach, H., and Coauthors, 2020: The ERA5 global reanalysis. *Quart. J. Roy. Meteor. Soc.*, **146**(730), 1999–2049, <https://doi.org/10.1002/qj.3803>.
- Honda, T., and Coauthors, 2018: Assimilating all-sky Himawari-8 satellite infrared radiances: A case of typhoon soudelor (2015). *Mon. Wea. Rev.*, **146**, 213–229, <https://doi.org/10.1175/MWR-D-16-0357.1>.
- Hong, S.-Y., and J.-O. J. Lim, 2006: The WRF single-moment 6-class microphysics scheme (WSM6). *Asia-Pacific Journal of Atmospheric Sciences*, **42**, 129–151.
- Iacono, M. J., E. J. Mlawer, S. A. Clough, and J.-J. Morcrette, 2000: Impact of an improved longwave radiation model, RRTM, on the energy budget and thermodynamic properties of the NCAR community climate model, CCM3. *J. Geophys. Res.*, **105**, 1 4873–1 4890, <https://doi.org/10.1029/2000JD900091>.

- Iacono, M. J., J. S. Delamere, E. J. Mlawer, and S. A. Clough, 2004: Development and evaluation of RRTMG_SW, a short-wave radiative transfer model for general circulation model applications. *Proc. Fourteenth ARM Science Team Meeting Proceedings*, Albuquerque, New Mexico.
- Kazumori, M., 2018: Assimilation of himawari-8 clear sky radiance data in JMA's global and mesoscale NWP systems. *J. Meteor. Soc. Japan*, **96**, 173–192, <https://doi.org/10.2151/jmsj.2018-037>.
- Lee, J.-R., J. Li, Z. L. Li, P. Wang, and J. L. Li, 2019: ABI water vapor radiance assimilation in a regional NWP Model by accounting for the surface impact. *Earth and Space Science*, **6**, 1652–1666, <https://doi.org/10.1029/2019EA000711>.
- Li, J., J. L. Li, J. Otkin, T. J. Schmit, and C.-Y. Liu, 2011: Warning information in a preconvection environment from the geostationary advanced infrared sounding system—A simulation study using the IHOP case. *J. Appl. Meteorol. Climatol.*, **50**, 776–783, <https://doi.org/10.1175/2010JAMC2441.1>.
- Li, X., X. L. Zou, and M. J. Zeng, 2019: An alternative bias correction scheme for CrIS data assimilation in a regional model. *Mon. Wea. Rev.*, **147**(3), 809–839, <https://doi.org/10.1175/MWR-D-18-0044.1>.
- Liu, J. J., H. Li, E. Kalnay, E. J. Kostelich, and I. Szunyogh, 2009: Univariate and multivariate assimilation of AIRS humidity retrievals with the local ensemble transform Kalman filter. *Mon. Wea. Rev.*, **137**, 3918–3932, <https://doi.org/10.1175/2009MWR2791.1>.
- Lu, J. Z., T. Feng, J. Li, Z. L. Cai, X. J. Xu, L. Li, and J. L. Li, 2019: Impact of assimilating himawari-8-derived layered precipitable water with varying cumulus and microphysics parameterization schemes on the simulation of typhoon hatu. *J. Geophys. Res.*, **124**(6), 3050–3071, <https://doi.org/10.1029/2018JD029364>.
- Lupu, C., and A. McNally, 2011: Assimilation of radiance products from geostationary satellites: 1-year report. EUMETSAT/ECMWF Fellowship Programme Res. Rep. 21, 27 pp.
- Ma, Z. Z., E. S. Maddy, B. L. Zhang, T. Zhu, and S. A. Boukhabara, 2017: Impact assessment of Himawari-8 AHI data assimilation in NCEP GDAS/GFS with GSI. *J. Atmos. Oceanic Technol.*, **34**, 797–815, <https://doi.org/10.1175/JTECH-D-16-0136.1>.
- Mass, C. F., D. Ovens, K. Westrick, and B. A. Colle, 2002: Does increasing horizontal resolution produce more skillful forecasts. *Bull. Amer. Meteor. Soc.*, **83**, 407–430, [https://doi.org/10.1175/1520-0477\(2002\)083<0407:DIHRPM>2.3.CO;2](https://doi.org/10.1175/1520-0477(2002)083<0407:DIHRPM>2.3.CO;2).
- Matricardi, M., F. Chevallier, G. Kelly, and J.-N. Thépaut, 2004: An improved general fast radiative transfer model for the assimilation of radiance observations. *Quart. J. Roy. Meteor. Soc.*, **130**, 153–173, <https://doi.org/10.1256/qj.02.181>.
- McNally, A. P., P. D. Watts, J. A. Smith, R. Engelen, G. A. Kelly, J. N. Thépaut, and M. Matricardi, 2006: The assimilation of AIRS radiance data at ECMWF. *Quart. J. Roy. Meteor. Soc.*, **132**(616), 935–957, <https://doi.org/10.1256/qj.04.171>.
- Min, M., and Coauthors, 2017: Developing the science product algorithm testbed for Chinese next-generation geostationary meteorological satellites: Fengyun-4 series. *Journal of Meteorological Research*, **31**(4), 708–719, <https://doi.org/10.1007/s13351-017-6161-z>.
- Okamoto, K., 2017: Evaluation of IR radiance simulation for all-sky assimilation of Himawari-8/AHI in a mesoscale NWP system. *Quart. J. Roy. Meteor. Soc.*, **143**, 1517–1527, <https://doi.org/10.1002/qj.3022>.
- Okamoto, K., Y. Sawada, and M. Kunii, 2019: Comparison of assimilating all-sky and clear-sky infrared radiances from Himawari-8 in a mesoscale system. *Quart. J. Roy. Meteor. Soc.*, **145**, 745–766, <https://doi.org/10.1002/qj.3463>.
- Otkin, J. A., and R. Potthast, 2019: Assimilation of all-sky SEVIRI infrared brightness temperatures in a regional-scale ensemble data assimilation system. *Mon. Wea. Rev.*, **147**, 4481–4509, <https://doi.org/10.1175/MWR-D-19-0133.1>.
- Qi, L. B., J. J. Wu, and C. H. Shi, 2020: Rethink on forecast focus of a torrential rainfall event at Jianghuai region. *Torrential Rain and Disasters*, **39**(6), 647–657, <https://doi.org/10.3969/j.issn.1004-9045.2020.06.013>. (in Chinese with English abstract)
- Qin, Z. K., and X. L. Zou, 2018: Direct assimilation of ABI infrared radiances in NWP models. *IEEE Journal of Selected Topics in Applied Earth Observations and Remote Sensing*, **11**, 2022–2033, <https://doi.org/10.1109/JSTARS.2018.2803810>.
- Qin, Z. K., X. L. Zou, and F. Z. Weng, 2013: Evaluating added benefits of assimilating GOES imager radiance data in GSI for coastal QPFs. *Mon. Wea. Rev.*, **141**, 75–92, <https://doi.org/10.1175/MWR-D-12-00079.1>.
- Saunders, R., M. Matricardi, and P. Brunel, 1999: An improved fast radiative transfer model for assimilation of satellite radiance observations. *Quart. J. Roy. Meteor. Soc.*, **125**, 1407–1425, <https://doi.org/10.1002/qj.1999.49712555615>.
- Schmit, T. J., M. M. Gunshor, W. P. Menzel, J. J. Gurka, J. Li, and A. S. Bachmeier, 2005: Introducing the next-generation advanced baseline imager on GOES-R. *Bull. Amer. Meteor. Soc.*, **86**, 1079–1096, <https://doi.org/10.1175/BAMS-86-8-1079>.
- Szyndel, M. D. E., G. Kelly, and J. N. Thépaut, 2005: Evaluation of potential benefit of assimilation of SEVIRI water vapour radiance data from Meteosat-8 into global numerical weather prediction analyses. *Atmospheric Science Letters*, **6**, 105–111, <https://doi.org/10.1002/asl.98>.
- Tewari, M., and Coauthors, 2004: Implementation and verification of the Unified NOAA land surface model in the WRF model. *Proc. 20th Conf. on Weather Analysis and Forecasting/16th Conf. on Numerical Weather Prediction*, Seattle, 11–15.
- Thépaut, J. N., 2003: Satellite data assimilation in numerical weather prediction: An overview. *Proc. ECMWF Seminar on Recent Developments in Data Assimilation for Atmosphere and Ocean*, Reading, UK, ECMWF, 75–96.
- Thompson, G., R. M. Rasmussen, and K. Manning, 2004: Explicit forecasts of winter precipitation using an improved bulk microphysics scheme. Part I: Description and sensitivity analysis. *Mon. Wea. Rev.*, **132**, 519–542, [https://doi.org/10.1175/1520-0493\(2004\)132<0519:EFOWPU>2.0.CO;2](https://doi.org/10.1175/1520-0493(2004)132<0519:EFOWPU>2.0.CO;2).
- Tiedtke, M., 1989: A comprehensive mass flux scheme for cumulus parameterization in large-scale models. *Mon. Wea. Rev.*, **117**, 1779–1800, [https://doi.org/10.1175/1520-0493\(1989\)117<1779:ACMFSF>2.0.CO;2](https://doi.org/10.1175/1520-0493(1989)117<1779:ACMFSF>2.0.CO;2).
- Wang, P., and Coauthors, 2015: Assimilation of thermodynamic information from advanced infrared sounders under partially cloudy skies for regional NWP. *J. Geophys. Res.*, **120**, 5469–5484, <https://doi.org/10.1002/2014JD022976>.
- Wang, X., M. Min, F. Wang, J. P. Guo, B. Li, and S. H. Tang, 2019: Intercomparisons of cloud mask products among Fengyun-4A, Himawari-8, and MODIS. *IEEE Trans. Geosci. Remote Sens.*, **57**(11), 8827–8839, <https://doi.org/10.1109/TGRS.2019.2923247>.

- Wang, Y. B., Z. Q. Liu, S. Yang, J. Z. Min, L. Q. Chen, Y. D. Chen, and T. Zhang, 2018: Added value of assimilating Himawari-8 AHI water vapor radiances on analyses and forecasts for “7.19” severe storm over North China. *J. Geophys. Res.*, **123**, 3374–3394, <https://doi.org/10.1002/2017JD027697>.
- Weng, F. Z., 2007: Advances in radiative transfer modeling in support of satellite data assimilation. *J. Atmos. Sci.*, **64**, 3799–3807, <https://doi.org/10.1175/2007JAS2112.1>.
- Weng, F. Z., X. W. Yu, Y. H. Duan, J. Yang, and J. J. Wang, 2020: Advanced radiative transfer modeling system (ARMS): A new-generation satellite observation operator developed for numerical weather prediction and remote sensing applications. *Adv. Atmos. Sci.*, **37**, 131–136, <https://doi.org/10.1007/s00376-019-9170-2>.
- Xu, D. M., Z. Q. Liu, X.-Y. Huang, J. Z. Min, and H. L. Wang, 2013: Impact of assimilating IASI radiance observations on forecasts of two tropical cyclones. *Meteorol. Atmos. Phys.*, **122**, 1–18, <https://doi.org/10.1007/s00703-013-0276-2>.
- Xu, D. M., Z. Q. Liu, S. Y. Fan, M. Chen, and F. F. Shen, 2021: Assimilating all-sky infrared radiances from Himawari-8 using the 3DVar method for the prediction of a severe storm over North China. *Adv. Atmos. Sci.*, **38**, 661–676, <https://doi.org/10.1007/s00376-020-0219-z>.
- Yang, J., Z. Q. Zhang, C. Y. Wei, F. Lu, and Q. Guo, 2017: Introducing the new generation of Chinese geostationary weather satellites, Fengyun-4. *Bull. Amer. Meteor. Soc.*, **98**, 1637–1658, <https://doi.org/10.1175/BAMS-D-16-0065.1>.
- Yin, R. Y., W. Han, Z. Q. Gao, and J. Li, 2021: Impact of high temporal resolution FY-4A geostationary interferometric infrared sounder (GIIRS) radiance measurements on typhoon forecasts: Maria (2018) case with GRAPES global 4D-var assimilation system. *Geophys. Res. Lett.*, **48**, e2021GL093672, <https://doi.org/10.1029/2021GL093672>.
- Zapotozny, T. H., J. A. Jung, J. F. Le Marshall, and R. E. Treadon, 2007: A two-season impact study of satellite and in situ data in the NCEP global data assimilation system. *Wea. Forecasting*, **22**, 887–909, <https://doi.org/10.1175/WAF1025.1>.
- Zhong, J.-Q., B. Lu, W. Wang, C.-C. Huang, and Y. Yang, 2020: Impact of soil moisture on winter 2-m temperature forecasts in northern China. *Journal of Hydrometeorology*, **21**, 597–614, <https://doi.org/10.1175/JHM-D-19-0060.1>.
- Zou, X. L., F. Z. Weng, and Z. K. Qin, 2017: Direct assimilation of AHI and ABI infrared radiances in NWP models. *Proc. 2017 IEEE International Geoscience and Remote Sensing Symposium*, Fort Worth, USA, IEEE, 290–292, <https://doi.org/10.1109/IGARSS.2017.8126952>.